ChemPubSoc Europe

DOI: 10.1002/cphc.201900363

CHEMPHYSCHEM Articles

Deuteron Solid-State NMR Relaxation Measurements Reveal Two Distinct Conformational Exchange Processes in the Disordered N-Terminal Domain of Amyloid-β Fibrils

Liliya Vugmeyster,*[a] Dan Fai Au,[a] Dmitry Ostrovsky,[b] and Riqiang Fu[c]

We employed deuterium solid-state NMR techniques under static conditions to discern the details of the μs–ms timescale motions in the flexible N-terminal subdomain of $A\beta_{1-40}$ amyloid fibrils, which spans residues 1–16. In particular, we utilized a rotating frame ($R_{1\rho}$) and the newly developed time domain quadrupolar Carr-Purcell-Meiboom-Gill (QCPMG) relaxation measurements at the selectively deuterated side chains of A2, H6, and G9. The two experiments are complementary in terms of probing somewhat different timescales of motions, governed by the tensor parameters and the sampling window of the magnetization decay curves. The results indicated two mobile "free" states of the N-terminal domain undergoing global diffusive motions, with isotropic diffusion coefficients of $0.7-1\cdot10^8$ and $0.3-3\cdot10^6 ad^2 s^{-1}$. The free states are also involved in the conformational exchange with a single bound state, in which the diffusive motions are quenched, likely due to transient interactions with the structured hydrophobic core. The conformational exchange rate constants are $2-3\cdot10^5\ s^{-1}$ and $2-3\cdot10^4\ s^{-1}$ for the fast and slow diffusion free states, respectively.

1. Introduction

Amyloid-β protein (Aβ) is one of the major components of neurotoxic amyloid plaques in the brains of patients with Alzheimer's disease.[1–2] Out of the different variants of Aβ, $A\beta_{1-40}$ is the most abundant.[2–3] The fibrils formed by this peptide are capable of forming different polymorphs that vary in cytotoxicity.[4–7] The 3-fold symmetric polymorph was shown to be significantly more toxic, especially in comparison with the 2-fold symmetric polymorph[1,8] In the fibrillar form, the peptide comprises two domains: the structured C-terminal domain forms a parallel in-register cross-β structure, while the N-terminal domain (residues 1–16) remains unstructured.[5,8–9] In fact, the resonance NMR assignments for wild-type Aβ start with residue 9.[5,8]

The N-terminal domain is known to be extremely important in regulating the overall aggregation of Aβ.[10–16] It contains the main binding and regulatory sites for interaction with metals[17–23] as well as several regulatory sites that have recently been implicated to be controlled via post-translational modifications..[14–15,24–27] Multiple works have revealed the flexibility of the N-terminal domain.[5–7,28–30,31,32–34,35–36] Site-specific studies of the dynamics of the insoluble aggregates of Aβ are rare due to challenges in obtaining the necessary resolution and sensitivity in the solid non-crystalline state.[28,37–42] Of note are the works of Fawzi et al.,[43–44] who utilized solution NMR saturation transfer approaches to probe the binding of monomeric Aβ to the surface of protofibrils and detected several states as part of the pathways of the binding of the monomer to protofibrils.

We have recently utilized ^2H solid-state static NMR approaches based on line shape analysis, longitudinal relaxation, and selected rotating frame relaxation measurements to investigate the site-specific side-chain dynamics of the N-terminal domain of $A\beta_{1-40}$ fibrils in the toxic 3-fold symmetric polymorph.[45] The data suggested a two-state model in which the free state of the domain undergoes a diffusive motion. This motion is quenched in the bound state, likely due to the transient interaction with the structured C-terminal domain. Line shape analysis led to the determination of the fraction of the bound state and diffusion coefficient, under the assumption of isotropic diffusion, for the side chains of A2, F4, H6, G9, and V12. The fraction of the bound state increases progressively along the sequence, with V12 already over 85% in the bound state at 37 °C. The diffusion coefficient decreases along the sequence, supporting the notion of the overall decreases in mobility along the N-terminal chain. Deuteron rotating frame relaxation measurements ($R_{1\rho}$) permitted us to determine the conformational exchange rate constant at the A2 site within the two-state model.

In this work, we utilize advanced deuteron static solid-state NMR approaches to probe the multitude of motional approaches in the side chains of the N-terminal domain. We use selective isotopic labeling approaches to probe three key side chains: A2, H6, and G9 (Figure 1). Our main NMR tools are the newly developed deuteron $R_{1\rho}$ measurements[45–46] as well as deuteron quadrupolar time domain Carr-Purcell-Meiboom-Gill (CPMG) measurements. While the analysis of quadrupolar CPMG

[a] Prof. L. Vugmeyster, D. F. Au
Department of Chemistry, University of Colorado Denver, Denver CO USA 80204
E-mail: liliya.vugmeyster@ucdenver.edu
[b] Dr. D. Ostrovsky
Department of Mathematics, University of Colorado Denver, Denver CO USA 80204
[c] Dr. R. Fu
National High Field Magnetic Laboratory, Tallahassee, FL 32310

Supporting information for this article is available on the WWW under https://doi.org/10.1002/cphc.201900363

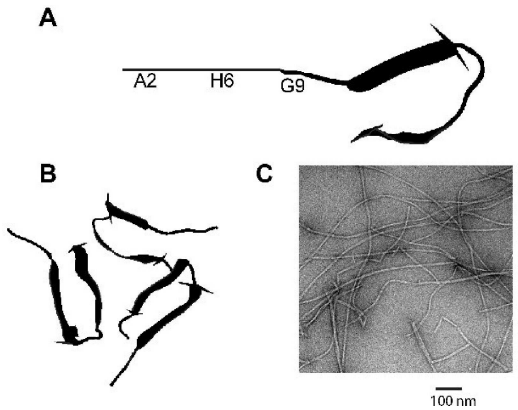

Figure 1. A) Schematic representation of $A\beta_{1-40}$ protein showing the positions of the residues probed in this work. The structure of the monomer for residues 9 and beyond is taken from the protein data bank file 2LMP.pdb,[4] while the rest of the N-terminal domain is shown schematically as a line. B) 3-fold symmetric fibril structure, top view.[4] C) A typical negatively stained transmission electron microscopy image of the fibrils in the 3-fold symmetric polymorph, shown for typical fibrils used in this study.

(QCPMG) line shapes is well known,[47] the time domain approach is applied for the first time here for studies of protein dynamics in a solid crystalline state to our knowledge. Both the $R_{1\rho}$ and the QCPMG approaches are sensitive to conformational exchange processes, but can probe somewhat different timescales.

The complementarity of the $R_{1\rho}$ and CPMG approaches are well known for solution NMR dynamics studies of proteins.[48] Recently, significant advancements have been achieved in the development of these techniques for proteins, and in particular for $^{15}N/^{13}C$ $R_{1\rho}$ relaxation measurements under magic angle spinning(MAS) conditions.[49–62] The advantage of deuterium is its exquisite sensitivity to motional processes and a relatively strong quadrupolar interaction in comparison to the dipolar network, which essentially transforms the problem into a single particle case.[63–64] Performing experiments under static conditions requires multiple samples for site specificity, but gains the advantage of foregoing sample rotation, which introduces additional time dependence into the Hamiltonian and requires more involved theory and simulations.[58,61] The combination of the two techniques for ^2H nuclei in the solid state permits us to reveal the presence of multiple dynamics processes in Aβ fibrils, with at least two distinct mobile states and one rigid (bound) state and two distinct timescales of conformational exchange between the flexible N-terminal domain and the more rigid C-terminal core domain.

2. Results and Discussion

2.1. Fibril Morphologies and Labeling Schemes

The goal of our work is to characterize in detail the μs-ms timescale motions in the flexible N-terminal domain of $A\beta_{1-40}$ fibrils in the 3-fold symmetric polymorph. The quaternary structure and a representative transmission electron microscopy image of the resulting fibrils are shown in Figure 1. Three key side chains along the flexible N-terminus, A2, H6, and G9, were deuterated with the labeling patterns summarized in Table 1. Each of the three samples of $A\beta_{1-40}$ contained deuteron labels in only ONE residue. Specifically, for the A2 residue, the methyl group was labeled. For the H6 residue, we utilized the τ-His modification ($-^{\beta}CH_2$-ring-N–CD_3) that, as we have previously shown,[45] does not alter the morphology of the fibrils but provides a convenient labeling site. For G9, there is no real side chain and the two C_α deuterons were labeled.

Table 1. Residue-specific side-chain labeling patterns, main local motional modes, and effective quadrupolar coupling tensor parameters: quadrupolar coupling constant C_q and asymmetry η.

Residue	Labeling pattern	Motional mode	Effective C_q and η in the free states	Effective C_q and η in the bound state
A2	$-C^{\beta}D_3$	methyl three-site jumps	$C_q = 55.5$ kHz, $\eta = 0$	$C_q = 55.5$ kHz, $\eta = 0$
H6	$-^{\beta}CH_2$-ring-N-CD_3 (i.e. τ–His)	ring flip for the free states (angle of 30.55° (between C^{β}–C^{γ} and CD_3–N^{ε})[65] and methyl three-site jumps for all states	$C_q = 32.5$ kHz, $\eta = 0.63$	$C_q = 53$ kHz, $\eta = 0$
G9	$-^{\alpha}CD_2$	Two-site jumps of CD_2 with tetrahedral geometry	$C_q = 77.6$ kHz, $\eta = 1$	$C_q = 77.6$ kHz, $\eta = 1$

2.2. Overview of the Model

Previous work involving ^2H line shape analysis has indicated significantly narrowed line shapes induced by solvation (Figure 2). Based on the temperature dependence of the static solid-state deuteron line shape and longitudinal relaxation data, as well as the ^2H $R_{1\rho}$ data at the A2 site, we have suggested a two-state model involving the free and bound states of the N-terminal domain, as discussed in the Introduction (cf. Figure 3). Within this model, the free state is assumed to undergo isotropic diffusion motion, leading to a narrow spectral component, and the bound state, in which the diffusion is quenched, adds a wide base to the otherwise narrow line. The relative fraction of the bound state increases along the N-terminal sequence. The decomposition into Lorentzian and non-Lorentzian components yields approximate fractions of the bound state of 8%, 10%, and 35% for A2, H6, and G9, respectively. The F4 and V12 side-chain sites, which were investigated with the line shape technique, were not included in this study. The dynamics at the V12 side-chain are considerably quenched, with the fraction of the bound state at 85%, while the F4 site was omitted due its relative proximity to the A2 site and similar line shapes at the physiological temperature. Also of note is that the mobility of G9 falls in line with the other residues and, thus, is not due to the absence of the side-chain (see also Figure S5 of Ref. [45]).

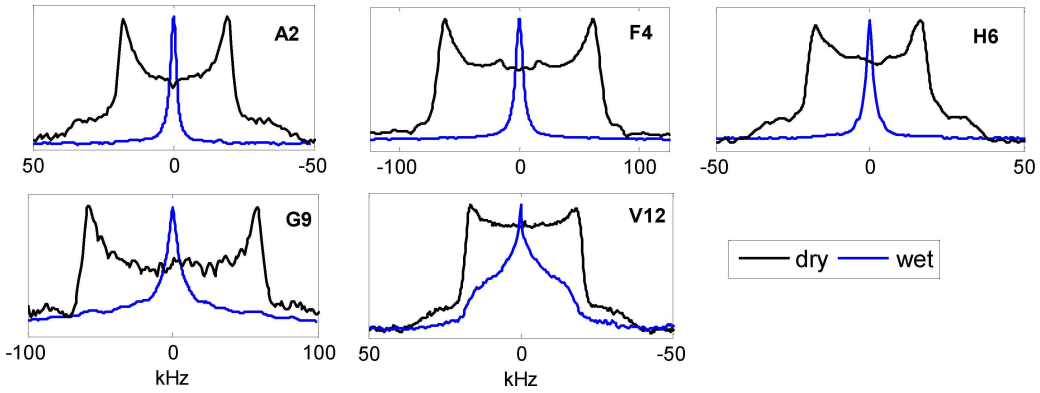

Figure 2. Comparison of the normalized ^{2}H static solid-state NMR line shapes for the dry (black) and hydrated (blue) states of the Aβ_{1-40} fibrils in the 3-fold symmetric polymorph, collected at 37 °C. Reprinted with permission from Au et al.,[45] license number 4552731304114.

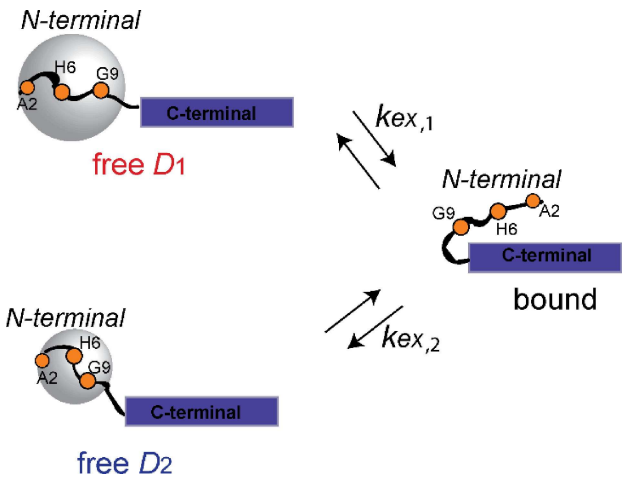

Figure 3. Schematic representation of the three-state motional model for the disordered N-terminal domain (residues 1–16) of Aβ_{1-40} fibrils. The N-terminal domain (curved line) transiently interacts with the structured C-terminal domain (blue rectangle). In the two free states, the N-terminal domain is assumed to undergo isotropic diffusion with the diffusion coefficients D_1 and D_2, $D_1 \gg D_2$, represented by the gray spheres, while in the bound state, the interactions quench this mode. The timescales of the interactions are given by the two chemical exchange rate constants, $k_{ex,1}$ and $k_{ex,2}$, respectively. The additional parameters of the model are the relative populations of all states. The location of the residues studied in this work is shown in orange. The patterns of the selective deuterium labels of the side chains are shown in Table 1.

The longitudinal relaxation data also delineated local modes of the side-chain motions, which in turn govern the effective tensor parameters, summarized in Table 1. In the free state, all of the local modes (methyl three-site jumps, ring flips of the histidine ring, two-site jumps of the $-CD_2$ group) are in the fast motional regime with respect to the quadrupolar coupling constant and, thus, effectively average the tensor in accordance with the symmetry properties of the motions. In the bound state, these motional regimes remain unchanged for A2 and G9; however, for H6, the histidine ring flips are no longer in the fast regime and do not contribute to tensor averaging.

Here, we combine ^{2}H $R_{1\rho}$ measurements under static conditions with time domain QCPMG measurements to probe slow fluctuations at the three key residues. The following detailed analysis will demonstrate that the dynamics are complex with two different free states detected, each with a distinct timescale of the diffusive motion and distinct chemical exchange constant with a single bound state. Note that the diffusion mode alone cannot explain the characteristic relaxation dispersion in either of these experiments (see Figure S7 in Ref. [45] for an example of the simulated relaxation dispersion curve for the $R_{1\rho}$ experiment in the absence of the conformational exchange).

2.3. The $R_{1\rho}$ Experiment

The ^{2}H $R_{1\rho}$ measurements under static conditions were performed as recently described,[46] with the pulse sequence shown in Figure 4. For hydrated protein powders, it is best to avoid spin-lock fields higher than 25–30 kHz and spin-lock times beyond 30 ms due to the possibility of temperature gradients throughout the sample. Additionally, the relatively low signal dictates the extent of the sampling of magnetization decay curves: in general, 12–17 delays were recorded with the lowest spin-lock time of 200 μs, at which point the spin lock is already effective and coherent oscillations are minimal. It is also of note that the magnetic field strength has a negligible effect on the resulting ^{2}H $R_{1\rho}$ relaxation parameters, as the quadrupolar interaction is not field-dependent.

Examples of the experimental magnetization decay curves $M(t)$ are shown in Figure 5. In all cases, the decay is not a single exponential. A double-exponential decay function was used for the analysis of the $R_{1\rho}$ relaxation for A2 and H6; however, for G9, the lower sensitivity of the samples precluded the determination of a slow-relaxing component and rather the decays were fitted to a single-exponential function with the baseline: $M(t) = Ae^{-t/T_{1\rho}} + B$. The results of the fits (Figure 6) indicate that the fast component for A2 and H6 is defined a lot more precisely and has a larger extent of dispersion with the change in the spin-lock field. The percentage of the fast-relaxing component is 65–70%. The single-exponential fit for the G9 component has a similar extent of precision and

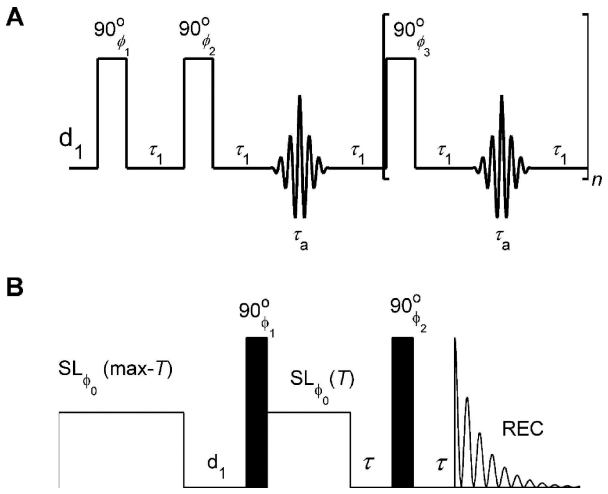

Figure 4. A) The QCPMG pulse sequence for ^{2}H nuclei. Quadrupolar echo block with the 90° pulses shown as rectangles is followed by a full echo acquisition period (τ_a) and then proceeds to an *n* repeating multiple echo unit (in square brackets). d_1 is the inter-scan delay, and τ_1 is the pulse ringing delay $\tau_{qcpmg} = \tau_a + 2\tau_1 + 90^\circ/2$. The analysis of decay curves starts with the first full echo in brackets. The following 16-step phase cycle is used: $\phi_1 = x,y,-x,-y$; $\phi_2 = y,x,y,x,-y,-x,-y,-x$; $\phi_3 = y,x,y,x,-y,-x,-y,-x$, $-y,-x,-y,-x$, y,x,y,x; $\phi_{rec} = -x,-y,x,y$. B) Pulse sequence for static ^{2}H solid-state $R_{1\rho}$ measurements.[46] The heat compensation block SL(max-*T*) is followed by the inter-scan delay d_1 and the preparation 90° pulse, followed by a variable spin-lock delay SL(*T*). The detection is accomplished using the quadrupole echo scheme, τ −90°−τ. The phase cycle corresponds to $\phi_0 = x$; $\phi_1 = -y,y$; $\phi_2 = -x,x$; receiver = −*y*,*y*.

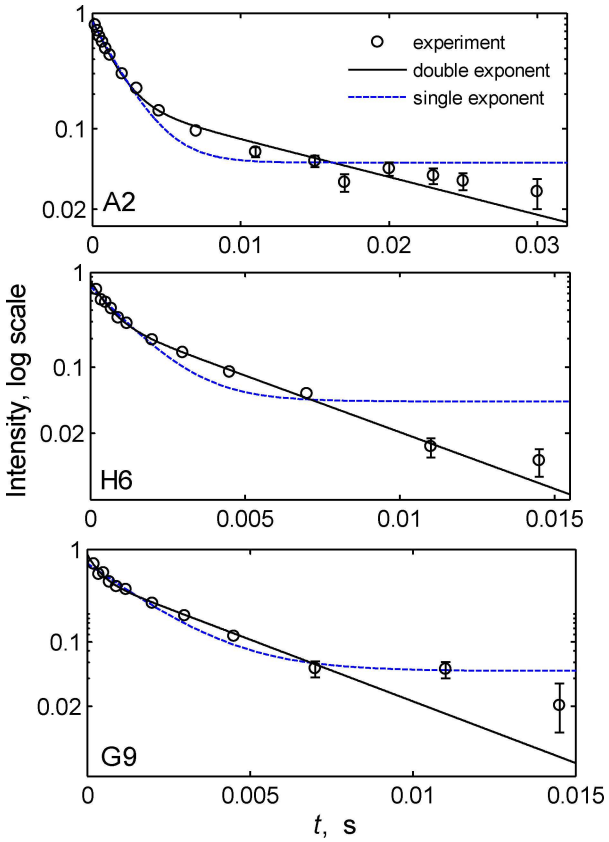

Figure 5. Examples of the experimental magnetization decay curves $M(t)$ obtained with the ^{2}H $R_{1\rho}$ pulse sequence of Figure 4B at a 10 kHz spin-lock field strength. Normalized peak intensities (shown on log scale), obtained via the integration of the central spectral component over the half-height region, versus time (circles). Blue lines represent the mono-exponential fits of the form $M(t) = Ae^{-t/T_{1\rho}} + B$, while the black lines represent the double-exponential fits. Data were collected at 37 °C with the field strength of 14. 1 T for A2 and H6 and 9.6 T for G9, for the selectively deuterated hydrated $A\beta_{1\text{-}40}$ fibrils in the 3-fold symmetric polymorph. Error bars smaller than the size of the symbols are not shown.

dispersion as the fast-relaxing component for the other two residues.

As the first step to understanding the underlying motional parameters, we thus focus on these more precisely defined components. We first invoke the model with a single free state and a single bound state to avoid overfitting the data and gain an insight into the general picture. The free state undergoes diffusive motions with a diffusion coefficient *D*, which is quenched in the bound state. The second motional mode is the exchange between the free and bound states with the rate constant k_{ex} and the fraction of the bound state p_{bound}. The starting parameters for p_{bound} have been taken from what has been determined on the basis of the line shape analysis.[45] The resulting fitting parameters of the model are shown in Table 2. For A2 and H6, the values of the diffusion coefficient are similar to what has been seen from the line shape analysis with $D = 3.5 \cdot 10^6$ rad^2 s^{-1} for A2 and $1 \cdot 10^6$ rad^2 s^{-1} for H6, and the k_{ex} values are $3 \cdot 10^4$ s^{-1} for both residues. However, for G9, the diffusion coefficient is orders of magnitude larger, $D = 7 \cdot 10^7$ rad^2/s, and the value of k_{ex} is also almost an order of magnitude larger at $2 \cdot 10^5$ s^{-1}. Given the fact that G9 is closer to the end of the N-terminal domain than either A2 or H6, it is not possible that this site is so much more mobile that the A2 and H6 sites. The most likely explanation is that due to the differences in the tensor parameters (Table 1) and higher fraction of the bound state ($p_{bound} = 0.36$ for G9 as opposed to 0.08 for A2), the $R_{1\rho}$ experiment is sensing a different, more mobile state for G9 compared with what is probed for A2 and H6. As we will see in the next section devoted to the QCPMG experiment, this hypothesis turns out to be true and the state is also seen for the other two residues.

Table 2. Fitting parameters (D, k_{ex}, p_{bound}) resulting from the static deuterium QCPMG and $R_{1\rho}$ experiments within two-state models of a single free and a single bound state. For $R_{1\rho}$, the fits to the fast-relaxing component are reported for A2 and H6. The colors indicate the different motional modes, with red corresponding to a fast diffusion and fast chemical exchange and blue to a slow diffusion and slow chemical exchange.

Residue	QCPMG	$R_{1\rho}$
A2	$D = 1 \cdot 10^8$ rad^2 s^{-1}; $k_{ex} = 3 \cdot 10^5$ s^{-1} $p_{bound} = 0.06$–0.1	$D = 3 \cdot 10^6$ rad^2 s^{-1}; $k_{ex} = 3 \cdot 10^4$ s^{-1} $p_{bound} = 0.06$–0.1
H6	$D = 1 \cdot 10^8$ rad^2 s^{-1}; $k_{ex} = 3 \cdot 10^5$ s^{-1} $p_{bound} = 0.12$–$0.0.18$	$D = 1 \cdot 10^6$ rad^2 s^{-1}; $k_{ex} = 3 \cdot 10^4$ s^{-1} $p_{bound} = 0.12$–0.18
G9	$D = 3 \cdot 10^5$ rad^2 s^{-1}; $k_{ex} = 2 \cdot 10^4$ s^{-1} $p_{bound} = 0.3$–0.4	$D = 7 \cdot 10^7$ rad^2 s^{-1}; $k_{ex} = 2 \cdot 10^5$ s^{-1} $p_{bound} = 0.3$–0.4

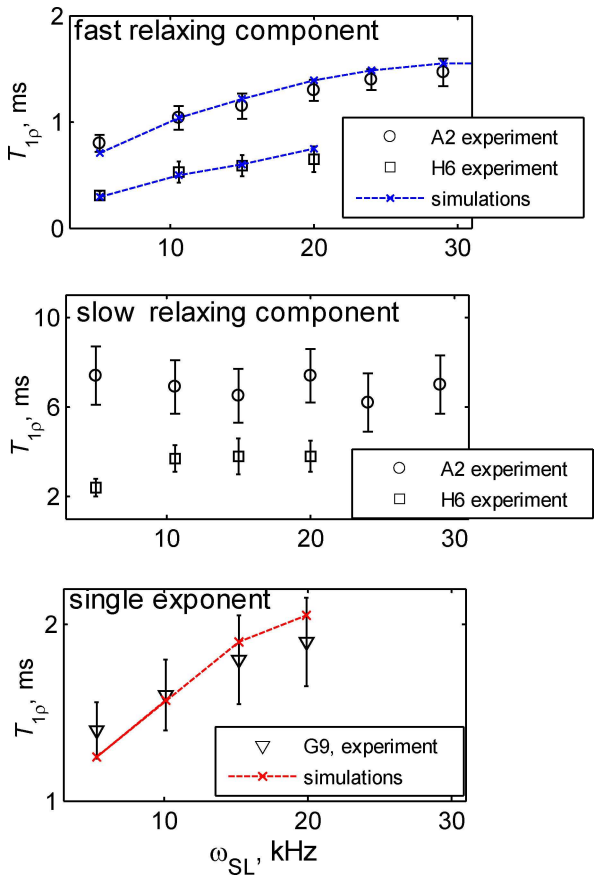

Figure 6. Experimental $T_{1\rho} = 1/R_{1\rho}$ relaxation times obtained from the double-exponential fits for A2 and H6 and single-exponential fit with the baseline for G9, as described in the text. –x– symbols represent simulations according to the two-site exchange model with one free and one bound state, with the parameters specified in Table 2. Note that within the full three-state model of Figure 3 for A2 and H6, the slow diffusion free state dominates relaxation and is denoted by blue, while for G9, the fast diffusion free state dominates relaxation and is denoted by red. Data were collected at 37 °C, with the field strength of 14.1 T for A2 and H6 and 9.6 T for G9.

It is also of note that the fitted values of the diffusion coefficients for A2 and H6 are somewhat higher than those from the line shape analysis, pointing to the extent of the anisotropy in the diffusion, as discussed in [45]. The sensitivity of the fits to the D and k_{ex} parameters is shown in Figure S1. The ranges of the fraction of the bound state consistent with the $R_{1\rho}$ data are specified in Table 2 and are consistent with what has been seen from the line shape analysis.

The existence of the slow-relaxing component for A2 and H6 (and the baseline for G9) is indicative of an additional motional state not seen by the fast-relaxing component. We have examined other possible sources of this slow component previously,[45] including diffusion anisotropy, explicit contributions from methyl jumps, and the effect of the dipolar proton network, and concluded that they are not expected to contribute substantially to the magnetization decay and cannot explain the second component. After the discussion of the results from the QCPMG experiment, which also probes this additional component, we will show how the full model involving two free states (Figure 3) can be used to explain the slow-relaxing $R_{1\rho}$ component.

2.4. The QCPMG Experiment

To further probe the us-ms timescale motions, we implemented the quadrupolar CPMG experiment.[66] This well-known technique has been applied for the sensitivity enhancement of the line shapes and detection of motions based on the line shape.[47,67–68] In this work, we use the time domain decays directly to obtain transverse relaxation parameters. Advances in the console technology (Bruker neoconsole) render the decay curves largely free of artifacts and thus permit this advancement. The pulse sequence is demonstrated in Figure 4 and consists of the acquisition of multiple full echoes. The key in probing motions is to obtain transverse relaxation rates as a function of pulse spacing, defined by $\tau_{qcpmg} = \tau_a + 2\tau_1 + 90^\circ/2$, with the details of the experiment specified in the legend of Figure 4 as well as in the Experimental Section. The number of echoes that can be acquired is limited by the amount of heating that the sample can tolerate and the temperature gradients in the sample acceptable for the dynamics study. For our hydrated fibril samples, we have found that 20 echoes is the limiting value after which the significant heating of the sample is observed. The minimal value of $\tau_{qcpmg}$is also limited by heating considerations as well as the ringing characteristics (dead time) of the setup. In principle, there are no inherent limitations on the maximum value of τ_{qcpmg} other than sufficiently long relaxation times to observe the signal. The minimum value of τ_{qcpmg} in our setup was 53 µs and the maximum value was 303 µs. With 20 echoes for $\tau_{qcpmg} = 53\ \mu s$, the total length of acquisition is about 1.1 ms, while with 15 echos for $\tau_{qcpmg} = 303\ \mu s$, the total length of acquisition is 4.5 ms. These "windows" define to what timescales of motions the experiment is most sensitive. Further, they can govern the unexpected T_2 relaxation dispersion profiles, as we will see below. Similar to the $R_{1\rho}$ measurements, the experiment is expected to be sensitive to conformational exchange processes. However, as we will show below, the interplay between the tensor parameters and sampling window of the time domain decays in the QCPMG measurements in comparison with the sampling limitations of the $R_{1\rho}$ technique lead to the complementarity of the two approaches in terms of their sensitivity to different motional modes.

Examples of the experimental time domain data collected with the multiple echo acquisition scheme are shown in Figure 7. Magnetization decay curves are then obtained by integrating the individual full echo patterns. Because the driving interaction is quadrupolar, the effects of the proton dipolar network are expected to be negligible. The data (not shown) collected in the presence of 75 kHz proton decoupling using the spinal64 scheme[69] yields decay curves indistinguishable from those in the absence of the decoupling and thus confirms this expectation. Within the experimental uncertainties, the decay curves are a single exponential and the resulting T_2 values as a function of τ_{qcpmg} are shown in Figure 8.

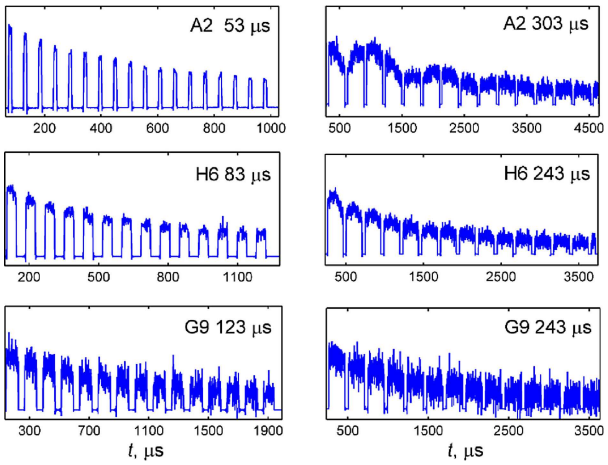

Figure 7. Examples of the experimental time domain data obtained with the ^{2}H QCPMG pulse sequence of Figure 4A, shown from the first echo in the loop (designated by the square brackets in the pulse sequence). Residue designation and echo times τ_{qcpmg} are shown directly on the panels. Collected at 14.1 T and 37 °C for the selectively deuterated Aβ_{1-40} fibrils in the 3-fold symmetric polymorph.

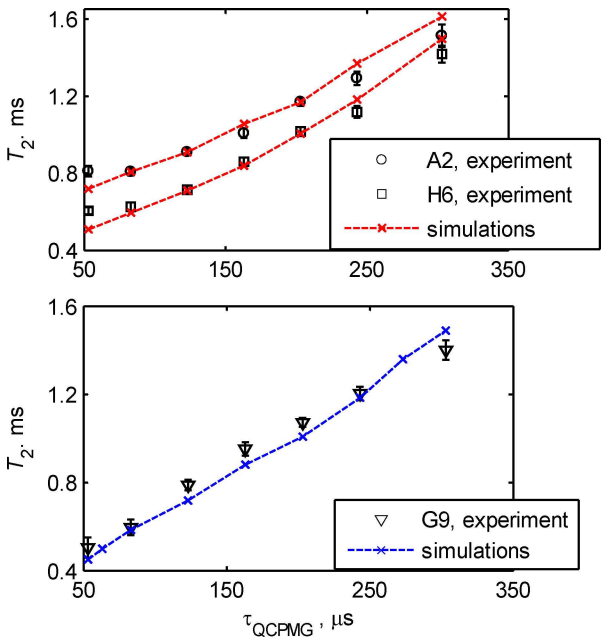

Figure 8. Transverse relaxation time T_2 as a function of τ_{qcpmg} obtained from the single-exponential fits of the magnetization decay curves for the A2 (circles), H6 (squares), and G9 (triangles) sites of the N-terminal domain of hydrated Aβ_{1-40} fibrils in the 3-fold symmetric polymorph, collected at 37 °C and 14.1 T. –x– symbols represent simulations according to the two-site exchange model with one free and one bound state, with the parameters specified in Table 2. Note that within the model of Figure 3 the fast diffusion free state dominates relaxation for A2 and H6 and is denoted by red, while for G9, the slow diffusion free state dominates relaxation and is denoted by blue.

Immediately apparent is a rather strong dispersion for all sites; however, the direction of this dispersion is the reverse of what is observed in the solution NMR CPMG dispersion profiles. One of the possible origins of this inversion is the anisotropic nature of the quadrupolar interactions coupled with the solid powder system and different length of the time domain acquisition for small and large τ_{qcpmg} values. Indeed, Tollinger et al.[62] already reported simulated CPMG relaxation dispersion profiles with "inverted" dispersions for ^{15}N backbone nuclei in a crystalline protein under MAS conditions when the main motional mechanism was assumed to be the reorientation of the anisotropic parts of the dipolar ^{15}N-^{1}H and ^{15}N CSA interactions, rather than the isotropic chemical shift interaction. Figure S2 explores this effect further using as an example simulations for the individual crystallites of the A2 methyl sites.

Analogously to the $R_{1\rho}$ data, QCPMG dispersion profiles are fitted to a model with a single free and a single bound state. The fitting parameters, listed in Table 2, show a rather interesting trend: for the A2 and H6 residues, the experiment now senses the free state with a fast diffusion constant of $1\cdot10^8$ rad^2/s and a fast chemical exchange constant of $3\cdot10^5$ s^{-1}, while for G9, it senses the free state with a slow isotropic diffusion of $3\cdot10^5$ rad^2/s and a slow k_{ex} of $2\cdot10^4$ s^{-1}. This trend is exactly opposite to what has been observed in the fits to the $R_{1\rho}$ data.

Thus, it appears that the two techniques are complementary to each other and point to the existence of two free states (Figure 3) of the N-terminal domain of the fibrils, one of which is significantly more mobile than the other. The next section will now integrate both these modes into a single model to determine the relative populations of the two free states. Figure S3 demonstrates the sensitivity of the QCPMG fits to the values of D and k_{ex} as well as demonstrates how either the fast or the slow motional mode fits the data. The relative fractions of the single free and bound states (Table 2) are similar to those seen from the $R_{1\rho}$ measurements. The fractions also agree with the results from the line shape decomposition.[45]

2.5. Discussion of the Full Model Involving Two Free States

It is evident from the combination of the $R_{1\rho}$ and QCPMG data that there are two distinct states present in the N-terminal subdomain of the fibrils (Figure 3). The first state is characterized by a very fast diffusion with a rate of the order of $D_1 = 0.7–1\cdot10^8$ rad^{2}s^{-1} and also participates in the conformational exchange with a rate constant of $k_{ex,1} = 2–3\cdot10^5$ s^{-1}. The second motional mode has a much slower diffusion, with the diffusion coefficient D_2 in the range of $3\cdot10^6$ to $3\cdot10^5$ rad^{2}s^{-1}, from A2 to G9, and participates in a different conformational exchange process with a rate constant of $k_{ex,2} = 2–3\cdot10^4$ s^{-1}. The nature of the conformational exchange with a single bound state likely originates from a transient interaction with the rigid C-terminal domain spanning the core of the fibrils. Our experiments do not differentiate between intermolecular and intramolecular interactions of the N-terminal domain with the structured core. The two free states detected here could be an approximation of a general ensemble of flexible states of the N-terminal subdomain. However, from our data, only two distinct states are visible.

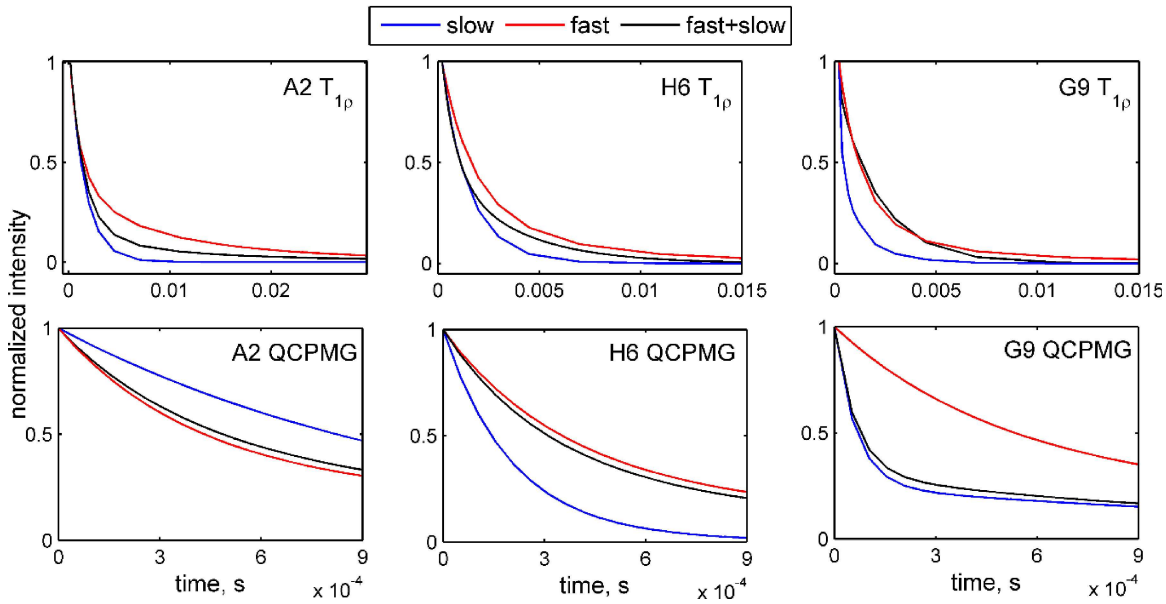

Figure 9. Simulated ^{2}H static $R_{1\rho}$ and QCPMG magnetization decay curves for either the two-state model with one free and one bound state (blue and red lines for the slow and fast diffusion states, respectively) or the full three-state model (black line, model as depicted in Figure 3). The diffusion coefficients D_1, D_2 and the rate constants $k_{ex,1}$ and $k_{ex,2}$ for the individual modes are specified in Table 2 as well as the relative fractions of the free and bound states. The relative fractions of the two free states are 25% of the slow diffusion state for A2, 35% for H6, and 95% for G9. $R_{1\rho}$ simulations are shown for the 15 kHz spin-lock field strength for A2 and H6 and 20 kHz for G9. QCPMG simulations are shown for $\tau_{qcpmg} = 53$ μs.

We then pose the question of whether the full model with the two free states can be analyzed in more detail to gain insight into how each of the modes is highlighted in either the QCPMG or the $R_{1\rho}$ experiment. This is explored in Figure 9, which demonstrates simulated data for the full model and its individual components. The key point here is that for the full model to be selectively sensitive to the individual motional modes, one has to use the relative fractions of the two free states as an additional fitting parameter. Thus, for the A2 residue with 25 ± 5% of the slow diffusion state, we can see that the $R_{1\rho}$ decay curve for the full model (Figure 9, in black) is close to the simulated data for the slow motional mode in the initial sampling of the curve (in blue), corresponding to the fast-relaxing component. This illustrates how the slow diffusion state is sensed by the fast-relaxing $R_{1\rho}$ component. For the QCPMG experiment, the full model almost coincides with the fast diffusion mode (in red) detected by the experiment. In fact, the slow-relaxing $R_{1\rho}$ component (with the experimental values shown in Figure 6, middle panel) provides an additional control for the values of the relative fractions of the free states. One can see from Figure 9 that the full model for the A2 $R_{1\rho}$ decay curve has a significant contribution from the slow-relaxing component for larger sampling times beyond 3 ms or so. The slow-relaxing component corresponds to the fast diffusion mode (Figure 9, in red). If the simulated data for the full model are fitted to the double-exponential function, the resulting two rates match the experimental values as well as the relative percentage of the fast-and slow-relaxing components in the experimental $R_{1\rho}$ data.

For the H6 residue, the fast diffusion state is sampled by the QCPMG experiment and the slow diffusion state by the fast-relaxing component of the $R_{1\rho}$ experiment, in analogy to A2. The relative percentage of the two free states has to be set at 35 ± 5% (slow diffusion state) to match the simulated decay curves to the modes detected by the experiment. Note that for the QCPMG decay curves, the fast diffusion state (in red) decays slower than the slow diffusion rate (in blue) for H6, while the trend is reversed in A2. For the G9 residue, the correspondence of the full model for the $R_{1\rho}$ curve to the fast diffusion mode (sensed by $R_{1\rho}$ in the experiment) is achieved only with a much higher percentage of the slow diffusion state, around 90–95%. The same percentage is required to match the full model to the slow diffusion mode for the QCPMG experiment for G9. Thus, the percentage of the slow diffusion state significantly increases toward the end of the N-terminal subdomain. It is important to emphasize that the magnetization between the two free states is effectively interconverted due to the exchange processes with the single bound state. Thus, even though for the G9 residue the population of the fast diffusion state is only 5–10%, on the timescale of the $R_{1\rho}$ relaxation (1–2 ms), almost all of the deuteron spins that originate from the slow diffusion state at a fixed point in time interconvert with the fast diffusion state (Figure S4). Further, the model of the two free states that are connected in consecutive fashion to the bound state rather than in parallel does not fit the data.

It is interesting to draw a parallel with the results found by Fawzi et al.[43–44] for the binding of monomeric Aβ to the surface of protofibrils, who utilized solution NMR dark saturation transfer approaches. They modeled the exchange dynamics with kinetic schemes involving two to three states, corresponding to the free monomer and the monomer-protofibril complexes with a differential extent of mobility. Thus, the existence

of multiple mobile states of the N-terminal domain undergoing transient interactions with the structured hydrophobic core could be a general property of the Aβ ensemble of monomers, protofibrils, oligomers, and fibrils.

3. Conclusions

From the methodological standpoint, it is important to emphasize the clear complementarity of the CPMG and $R_{1\rho}$ approaches for studies of the dynamics in the solid state in complex systems in which multiple motional modes are expected. In our case, the quadrupole interaction inherent to ^{2}H nuclei enabled quantitative studies of dynamics in which motional modes can be modeled explicitly and motional parameters determined from simulations of magnetization decay curves. The observed timescales in each experiment are dependent on the tensor parameters and the details of the sampling of the magnetization decay curves. If desired, the treatment can be extended to the model-free type modeling often employed for studies of protein dynamics. In most cases the full Liouvillian analysis is expected to be necessary. For single-labeled samples, the time domain QCPMG experiment provides an attractive alternative to the spectral domain acquisition, allowing for a significant reduction in data collection time.

Based on these two complementary approaches as well as previous studies of line shapes and longitudinal relaxation, the following picture emerged for the dynamics of the flexible N-terminal domain of $A\beta_{1-40}$ fibrils. At least two mobile states are present (Figure 3), for which overall mobility can be modeled within the isotropic diffusion approximation with coefficients in the range of $0.7-1\cdot10^8$ (fast state) and $0.3-3\cdot10^6$ rad^2 s^{-1} (slow state). For the slow state, the diffusion coefficient is the largest at the N-terminal residues and decreases along the sequence. The percentage of the slow state significantly increases toward the end of the N-terminal, with 25% for the A2 residue (probed at the $-CD_3$), 35% for the H6 residue (probed at the τ-His $-CD_3$ position), and 95% for the G9 residue (probed at the $-CD_2$ group). Each of these states undergoes a separate conformational exchange process with a single bound state, the nature of which is likely a transient interaction with a more rigid C-terminal domain spanning the core of the fibrils. The conformational exchange rate constants are $2–3\cdot10^5$ s^{-1} and $2–3\cdot10^4$ s^{-1} for the fast and slow diffusion free states, respectively and the relative fractions of the bound states are 8, 15, and 36% for A2, H6, and G9, respectively.

Due to the differences in the tensor parameters (defined by the local motional modes) and the fractions of the bound state, the fast diffusion state was most visible by the ^{2}H QCPMG measurement for A2 and H6 and by the $R_{1\rho}$ measurement for G9; the picture was reversed for the slow motional mode. In principle, the two free states detected here could be an approximation to a general ensemble of the flexible states of the N-terminal subdomain of Aβ fibrils. However, from our data, only two distinct states are visible.

Experimental Section

Sample Preparation

Samples of $A\beta_{1-40}$ in the twisted/3-fold symmetric polymorph were prepared as described in[40,45] starting with synthetic peptides, which incorporated selectively labeled amino acids and utilizing established protocols.[5,8] Their morphologies were confirmed by transmission electron microscopies and are shown in more details in[45] A hydrated state with a water content of 200% by weight was achieved by exposing lyophilized powder to water vapor in a sealed chamber at 25 °C until the water content reached saturation levels corresponding to about 40% by weight, followed by pipetting the remaining water by using deuterium-depleted H_2O. The samples were packed in 5 mm NMR tubes (cut to 21 mm length) using Teflon tape to center the sample volume in the coil of the NMR probe.

NMR Methods

Experiments were performed on 9.6 T (University of Colorado at Denver) and 14.1 T (National High Magnetic Field Laboratory) spectrometers equipped with the Bruker neoconsoles and static probes with 5 mm diameter coils: the wide-line low-E probe[70] for the 14.1 T spectrometer and the Phoenix probe for the 9.6 T spectrometer.

^{2}H QCPMG measurements[71] were performed at a 14.1 T field strength. The multiple echo acquisition approach utilized the pulse sequence similar to the one developed for half-integer quadrupolar spins,[66,71] as depicted in Figure 4. The measurements were performed with echo times (τ_{qcpmg}) between 53 and 303 μs with the rf irradiation frequency set exactly on resonance. 15 to 20 echoes were collected, and the restriction in the number of echoes originates from the sample heating effects. The number of scans varied between 4096 and 6144 depending on the signal-to-noise ratio in each sample. The inter-scan delay was set to 0.2–0.4 sec and 32 dummy scans were utilized. Integrated echo intensities were fitted to a single-exponential function with no offset. The 90° pulses corresponded to 1.8–2 μs and thus the effect of pulse imperfections is expected to be minimal.

The $R_{1\rho}$ methodology is described in previous work[46] with the pulse sequence shown in Figure 4, which utilizes the quadrupolar echo detection scheme with a two-step phase cycle.[63] The calibration of the spin-lock field strength was performed using a similar pulse sequence in which the spin-lock period was followed by a nutation pulse with a 90° phase shift. The duration of this pulse varied, and the zero-crossing of the signal was observed when the nutation corresponds to the π/2 pulse. Quadrupolar echo τ_{echo} delay was set to 31 μs. Spin-lock times varied between 200 μs and 15 ms (10–17 relaxation delays) and powers ranged between 5 and 30 kHz. 16–32 dummy scans were utilized. The number of scans varied depending on the signal obtained for each sample and each spin-lock field and ranged between 1000 and 9000 scans. To maintain a constant temperature throughout the experiment, it was necessary to equalize the amount of heating due to the variable RF power and spin-lock times. Within the same spin-lock field strength measurements, the heat compensation block ensures the same amount of heating throughout all delays. However, it is somewhat harder to account for the variations in heating with the variable spin-lock strength. Our approach was to use an internal thermometer based on the T_1 values in the presence of a "dummy" spin-lock heat compensation block using a sample with T_1 values very sensitive to temperature changes. We used a dimethyl-sulfone sample. Corrections in the effective sample temperatures can be made by varying the recycle delay in such a manner that the same

T_1 values are obtained with the dummy spin-lock field at all spin-lock field strengths. As a first approximation, we assumed that the heating effects will be similar in all samples within this relatively narrow rf power range. As the result of this calibration procedure, the recycle delay varied between 0.75 s at the lowest spin-lock field of 5 kHz to 2.3 s at the spin-lock field of 20 kHz, and 3.2 s at 29 kHz. The relaxation decay curves corresponding to the integration of the central narrow component (up to the half-height intensity) were fitted to either a single-exponential function with an offset (for G9), $M(t) = Ae^{-t/T_{1\rho}} + B$, or a double-exponential function (A2, H6).

Motional Modeling

The isotropic diffusion of the free state was modeled as discrete nearest-neighbor jumps on the surface of a sphere, using 192 sites with the DistMesh program[72] for the discretization of the Smoluchowski equation. The jump rate was the same for all pairs of sites and was selected to match the second non-zero eigenvalue of the diffusion operator (corresponding to the second-order Legendre polynomial eigenfunction) to be 6*D*, as described in detail in the Supporting Information of[45] The parameters of the quadrupolar tensors, quadrupolar coupling constant C_q, and tensor asymmetry η[63] for each type or residue in the free and bound states are listed in Table 1 and were derived from the corresponding local motional modes. An additional mode of exchange between one free and one bound state was accomplished by the introduction of one additional site with an arbitrary fixed angular position in the crystal-fixed frame. The exchange was modeled by jumps between every site describing the spherical diffusion and bound-state site. The relative weights of each site were expressed through the ratio of the forward and reverse rate constants for the exchange process. Modeling the exchange with two free states and one bound state (Figure 3) included two sets of 192 sites describing the surface of a sphere with the corresponding nearest-neighbor jump constants within each set as well as independent exchange constants between every site of each of the two sets and an arbitrarily fixed site in the crystal-fixed frame corresponding to the bound state. Simulated decays utilized time points identical to those used in the experiment. QCPMG time domain evolution includes the full Liouvillian treatment. $R_{1\rho}$ simulations for A2 were performed in the Redfield limit[73] due to the narrow line shapes and small fraction bound. We checked that the full Liouvillian treatment renders negligible changes to the results. $R_{1\rho}$ simulations for the H6 and G9 residues utilized the full Liouvillian treatment, as described in.[46] The number of crystallites used was governed by the fraction of the bound state in each residue and corresponded to 90 for A2 and 250 for H6 and G9. We checked that the increase in the number of crystallites beyond these values did not affect the resulting rates. All simulations were performed in Matlab and utilized selected blocks from the EXPRESS program.[74]

Acknowledgements

This work was supported by a National Institutes of Health Grant 1R15-GM111681 and NSF grant 1726947. Some of the experiments were performed at the National High Magnetic Field Laboratory, which is supported by NSF Cooperative Agreement NSF/DMR-1644779, the State of Florida, and the U.S. Department of Energy. We thank Jochem Struppe from Bruker Biospin for help with coding the QCPMG pulse sequences for the neoconsole.

Conflict of Interest

The authors declare no conflict of interest.

Keywords: amyloid fibrils · CPMG relaxation · quadrupolar interactions · rotating frame relaxation · solid-state NMR

[1] A. K. Paravastu, I. Qahwash, R. D. Leapman, S. C. Meredith, R. Tycko, *Proc. Natl. Aca. Sci. U.S.A.* **2009**, *106*, 7443–7448.
[2] E. Hubin, N. A. J. van Nuland, K. Broersen, K. Pauwels, *Cell. Mol. Life Sci.* **2014**, *71*, 3507–3521.
[3] J. T. Jarrett, E. P. Berger, P. T. Lansbury, Jr., *Ann. N. Y. Acad. Sci.* **1993**, *695*, 144–148.
[4] A. K. Paravastu, R. D. Leapman, W. M. Yau, R. Tycko, *Proc. Natl. Aca. Sci. U.S.A.* **2008**, *105*, 18349–18354.
[5] A. T. Petkova, W. M. Yau, R. Tycko, *Biochemistry* **2006**, *45*, 498–512.
[6] I. Bertini, L. Gonnelli, C. Luchinat, J. Mao, A. Nesi, *J. Am. Chem. Soc.* **2011**, *133*, 16013–16022.
[7] T. Luhrs, C. Ritter, M. Adrian, D. Riek-Loher, B. Bohrmann, H. Doeli, D. Schubert, R. Riek, *Proc. Natl. Acad. Sci. USA* **2005**, *102*, 17342–17347.
[8] A. T. Petkova, R. D. Leapman, Z. H. Guo, W. M. Yau, M. P. Mattson, R. Tycko, *Science* **2005**, *307*, 262–265.
[9] A. K. Paravastu, A. T. Petkova, R. Tycko, *Biophys. J.* **2006**, *90*, 4618–4629.
[10] S. Mazzitelli, F. Filipello, M. Rasile, E. Lauranzano, C. Starvaggi-Cucuzza, M. Tamborini, D. Pozzi, I. Barajon, T. Giorgino, A. Natalello, M. Matteoli, *Acta. Neuropath. Comm.* **2016**, *4*, 110.
[11] K. Brannstrom, A. Ohman, L. Nilsson, M. Pihl, L. Sandblad, A. Olofsson, *J. Am. Chem. Soc.* **2014**, *136*, 10956–10964.
[12] C. Morris, S. Cupples, T. W. Kent, E. A. Elbassal, E. P. Wojcikiewicz, P. Yi, D. Du, *Chemistry* **2018**, *24*, 9494–9498.
[13] J. M. Nussbaum, S. Schilling, H. Cynis, A. Silva, E. Swanson, T. Wangsanut, K. Tayler, B. Wiltgen, A. Hatami, R. Ronicke, K. Reymann, B. Hutter-Paier, A. Alexandru, W. Jagla, S. Graubner, C. G. Glabe, H. U. Demuth, G. S. Bloom, *Nature* **2012**, *485*, 651–655.
[14] M. P. Kummer, M. Hermes, A. Delekarte, T. Hammerschmidt, S. Kumar, D. Terwel, J. Walter, H. C. Pape, S. Konig, S. Roeber, F. Jessen, T. Klockgether, M. Korte, M. T. Heneka, *Neuron* **2011**, *71*, 833–844.
[15] N. Rezaei-Ghaleh, M. Amininasab, S. Kumar, J. Walter, M. Zweckstetter, *Nat. Commun.* **2016**, *7*, 11359.
[16] L. Xu, R. Nussinov, B. Ma, *Chem. Commun.* **2016**, *52*, 1733–1736.
[17] A. N. Istrate, S. A. Kozin, S. S. Zhokhov, A. B. Mantsyzov, O. I. Kechko, A. Pastore, A. A. Makarov, V. I. Polshakov, *Sci. Rep.* **2016**, *6*, 21734.
[18] A. I. Bush, *J. Alzheimer's Dis.* **2013**, *33*, S277–S281.
[19] Y. Miller, B. Y. Ma, R. Nussinov, *Coord. Chem.* **2012**, *256*, 2245–2252.
[20] V. Tougu, A. Tiiman, P. Palumaa, *Metallomics* **2011**, *3*, 250–261.
[21] T. Miura, M. Yoda, C. Tsutsumi, K. Murayama, H. Takeuchi, *J Pharm. Soc. Japan* **2010**, *130*, 495–501.
[22] T. Miura, K. Suzuki, N. Kohata, H. Takeuchi, *Biochemistry* **2000**, *39*, 7024–7031.
[23] A. A. Kulikova, A. A. Makarov, S. A. Kozin, *Mol. Biol.* **2015**, *49*, 217–230.
[24] M. P. Kummer, M. T. Heneka, *Alzheim. Reser. Ther.* **2014**, *6*.
[25] N. Rezaei-Ghaleh, S. Kumar, J. Walter, M. Zweckstetter, *J. Biol. Chem.* **2016**.
[26] Z.-W. Hu, M.-R. Ma, Y.-X. Chen, Y.-F. Zhao, W. Qiang, Y.-M. Li, *J. Biol. Chem.* **2017**, *292*, 2611–2623.
[27] S. Jawhar, O. Wirths, T. A. Bayer, *J. Biol. Chem.* **2011**, *286*, 38825–38832.
[28] H. A. Scheidt, I. Morgado, S. Rothemund, D. Huster, *J. Biol. Chem.* **2012**, *287*, 2017–2021.
[29] A. Olofsson, A. E. Sauer-Eriksson, A. Ohman, *J. Biol. Chem.* **2006**, *281*, 477–483.
[30] N. A. Whittemore, R. Mishra, I. Kheterpal, A. D. Williams, R. Wetzel, E. H. Serpersu, *Biochemistry* **2005**, *44*, 4434–4441.
[31] M. Torok, S. Milton, R. Kayed, P. Wu, T. McIntire, C. G. Glabe, R. Langen, *J. Biol. Chem.* **2002**, *277*, 40810–40815.
[32] I. Kheterpal, S. Zhou, K. D. Cook, R. Wetzel, *Proc. Natl. Acad. Sci. USA* **2000**, *97*, 13597–13601.
[33] S. S. S. Wang, S. A. Tobler, T. A. Good, E. J. Fernandez, *Biochemistry* **2003**, *42*, 9507–9514.
[34] I. Kheterpal, M. Chen, K. D. Cook, R. Wetzel, *J. Mol. Biol.* **2006**, *361*, 785–795.

[35] M. R. Sawaya, S. Sambashivan, R. Nelson, M. I. Ivanova, S. A. Sievers, M. I. Apostol, M. J. Thompson, M. Balbirnie, J. J. W. Wiltzius, H. T. McFarlane, A. O. Madsen, C. Riekel, D. Eisenberg, *Nature* **2007**, *447*, 453–457.
[36] H. Liu, C. Morris, R. Lantz, T. W. Kent, E. A. Elbassal, E. P. Wojcikiewicz, D. Du, *Angew. Chem. Int. Ed.* **2018**, *57*, 8017–8021; *Angew. Chem.* **2018**, *130*, 8149–8153.
[37] R. Linser, R. Sarkar, A. Krushelnitzky, A. Mainz, B. Reif, *J. Biomol. NMR* **2014**, *59*, 1–14.
[38] L. Vugmeyster, D. Ostrovsky, G. L. Hoatson, W. Qiang, B. I. Falconer, *J. Phys. Chem. B* **2017**, *121*, 7267–7275.
[39] L. Vugmeyster, D. Ostrovsky, M. A. Clark, B. I. Falconer, G. L. Hoatson, W. Qiang, *Biophys. J.* **2016**, *111*, 2135–2148.
[40] L. Vugmeyster, M. A. Clark, B. I. Falconer, D. Ostrovsky, D. Gantz, W. Qiang, G. L. Hoatson, *J. Biol. Chem.* **2016**, *291*, 18484–18495.
[41] T. K. Karamanos, A. P. Kalverda, G. S. Thompson, S. E. Radford, *Prog. Nucl. Magn. Reson. Spectrosc.* **2015**, *88–89*, 86–104.
[42] T. Wang, H. Jo, W. F. DeGrado, M. Hong, *J. Am. Chem. Soc.* **2017**.
[43] N. L. Fawzi, D. S. Libich, J. Ying, V. Tugarinov, G. M. Clore, *Angew. Chem.* **2014**, *53*, 10345–10349.
[44] N. L. Fawzi, J. Ying, R. Ghirlando, D. A. Torchia, G. M. Clore, *Nature* **2011**, *480*, 268–272.
[45] D. F. Au, D. Ostrovsky, R. Fu, L. Vugmeyster, *J. Biol. Chem.* **2019**, *294*, 5840–5853.
[46] L. Vugmeyster, D. Ostrovsky, *ChemPhysChem* **2019**, *20*, 333–342.
[47] F. H. Larsen, *Annual Reports on Nmr Spectroscopy, Vol 71, Vol. 71*, **2010**, pp. 103–137.
[48] A. G. Palmer, 3rd, *J. Magn. Reson.* **2014**, *241*, 3–17.
[49] N.-A. Lakomek, S. Penzel, A. Lends, R. Cadalbert, M. Ernst, B. Meier, *Chemistry* **2017**, *23*, 9425–9433.
[50] A. Krushelnitsky, T. Zinkevich, B. Reif, K. Saalwächter, *J. Magn. Reson.* **2014**, *248*, 8–12.
[51] V. Kurauskas, S. A. Izmailov, O. N. Rogacheva, A. Hessel, I. Ayala, J. Woodhouse, A. Shilova, Y. Xue, T. Yuwen, N. Coquelle, J.-P. Colletier, N. R. Skrynnikov, P. Schanda, *Nat. Commun.* **2017**, *8*, 145.
[52] C. Quinn, A. McDermott, *J. Biomol. NMR* **2009**, *45*, 5–8.
[53] P. Ma, J. D. Haller, J. Zajakala, P. Macek, A. C. Sivertsen, D. Willbold, J. Boisbouvier, P. Schanda, *Angew. Chem. Int. Ed.* **2014**, *53*, 4312–4317; *Angew. Chem.* **2014**, *126*, 4400–4405.
[54] C. M. Quinn, A. E. McDermott, *J. Biomol. NMR* **2012**, *222*, 1–7.
[55] D. F. Gauto, A. Hessel, P. Rovó, V. Kurauskas, R. Linser, P. Schanda, *Solid State Nucl. Magn. Reson.* **2017**, *87*, 86–95.
[56] P. Rovó, R. Linser, *ChemPhysChem* **2018**, *19*, 34–39.
[57] P. Rovó, R. Linser, *J. Phys. Chem. B* **2017**, *121*, 6117–6130.
[58] A. Krushelnitsky, D. Gauto, D. C. Rodriguez Camargo, P. Schanda, K. Saalwachter, *J. Biomol. NMR* **2018**, *71*, 53–67.
[59] M. Shannon, T. Theint, D. Mukhopadhyay, K. Surewicz, W. Surewicz, D. Marion, P. Schanda, C. P. Jaroniec, *ChemPhysChem*.
[60] A. A. Smith, E. Testori, R. Cadalbert, B. H. Meier, M. Ernst, *J. Biomol. NMR* **2016**, *65*, 171–191.
[61] P. Schanda, M. Ernst, *Prog. Nucl. Magn. Reson. Spectrosc.* **2016**, *96*, 1–46.
[62] M. Tollinger, A. C. Sivertsen, B. H. Meier, M. Ernst, P. Schanda, *J. Am. Chem. Soc.* **2012**, *134*, 14800–14807.
[63] R. L. Vold, R. R. Vold, *Advances in Magnetic and Optical Resonance, Vol. 16* (Ed.: W. Warren), Acadenic Press, San Diego, **1991**, pp. 85–171.
[64] R. R. Vold, *Nuclear Magnetic Resonance Probes of Molecular Dynamics* (Ed.: R. Tycko), Kluwer academic Publishers, Dordrecht, **1994**, pp. 27–112.
[65] M. Malinska, M. Dauter, M. Kowiel, M. Jaskolski, Z. Dauter, *Acta Crystallogr. Sect. D* **2015**, *71*, 1444–1454.
[66] F. H. Larsen, H. J. Jakobsen, P. D. Ellis, N. C. Nielsen, *J. Phys. Chem. A* **1997**, *101*, 8597–8606.
[67] L. Vugmeyster, D. Ostrovsky, *Methods* **2018**, *148*, 136–145.
[68] R. L. Vold, G. L. Hoatson, L. Vugmeyster, D. Ostrovsky, P. J. De Castro, *Phys. Chem. Chem. Phys.* **2009**, *11*, 7008–7012.
[69] B. M. Fung, A. K. Khitrin, K. Ermolaev, *J. Magn. Reson.* **2000**, *142*, 97–101.
[70] P. L. Gor'kov, E. Y. Chekmenev, C. Li, M. Cotten, J. J. Buffy, N. J. Traaseth, G. Veglia, W. W. Brey, *J. Magn. Reson.* **2007**, *185*, 77–93.
[71] F. H. Larsen, H. J. Jakobsen, P. D. Ellis, N. C. Nielsen, *Mol. Phys.* **1998**, *95*, 1185–1195.
[72] P.-O. Persson, G. Strang, *SIAM Rev.* **2004**, *46*, 329–345.
[73] A. Abragam, *Principles of Nuclear Magnetism*, Clarendon Press, Oxford, **1961**.
[74] R. L. Vold, G. L. Hoatson, *J. Magn. Reson.* **2009**, *198*, 57–72.

Manuscript received: April 11, 2019
Revised manuscript received: May 12, 2019
Accepted manuscript online: May 14, 2019
Version of record online: June 14, 2019